Highly durable electrocatalyst with low-loading platinum-cobalt nanoparticles dispersed over single-atom Co-N-Graphene nanofiber for efficient fuel cell

Lina Chong[1,*], Jianguo Wen[2,*], Zhenzhen Yang[1], Yulin Lin[2], Ira D. Bloom[1], Daniel Abraham[1,*]

Supplementary Information

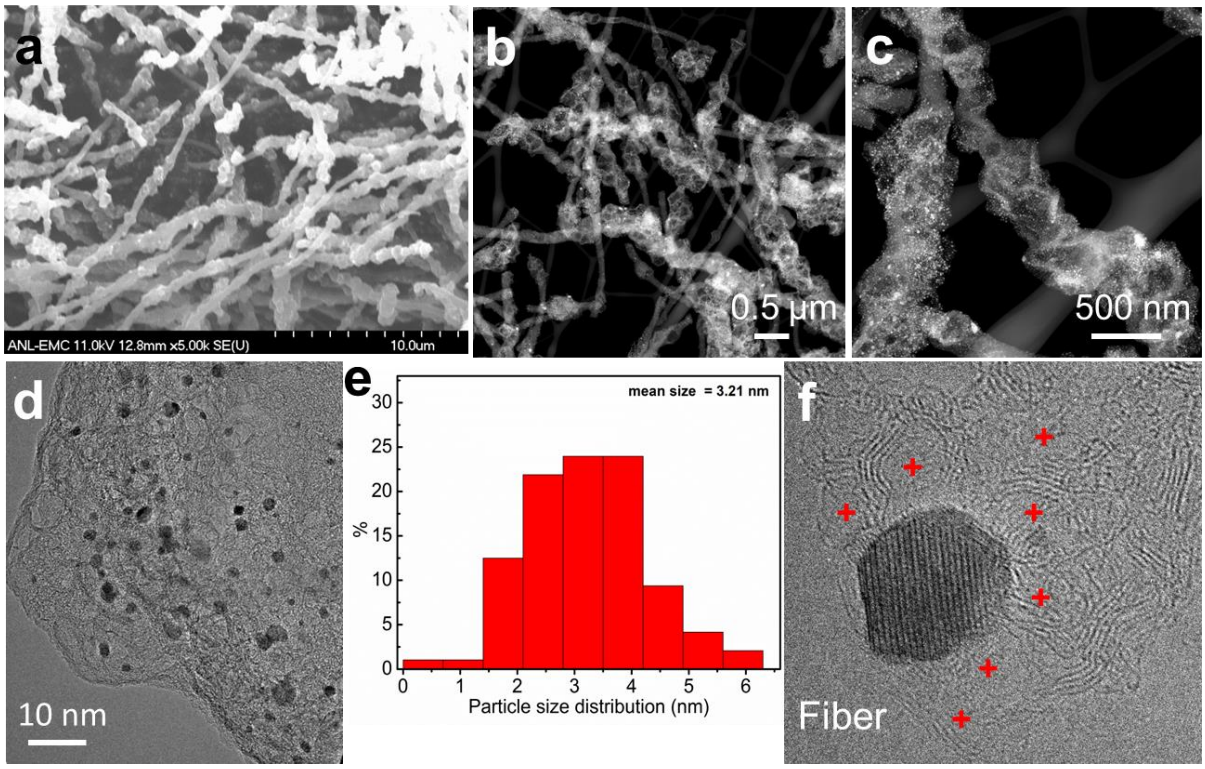

Supplementary Fig. 1 | (**a**) SEM image of CoMOF/PAN fiber. The MOF crystals are connected by PAN fiber. The diameter of the CoMOF/PAN fiber is around ~ 500 nm. (**b**) and (**c**) TEM images of LPCNGF, showing "beads" connected by "string". Individual fiber has an average diameter of ~ 300 nm. The beads were converted from the Co-MOF maintaining the MOF structure. (**d**) HRTEM image of LPCNGF. (**e**) Particle size distribution. (**f**) HRTEM image of LPCNGF from "string" part, showing the high graphitization and the graphene layers, as well as the abundant meso-pores (red crosses).

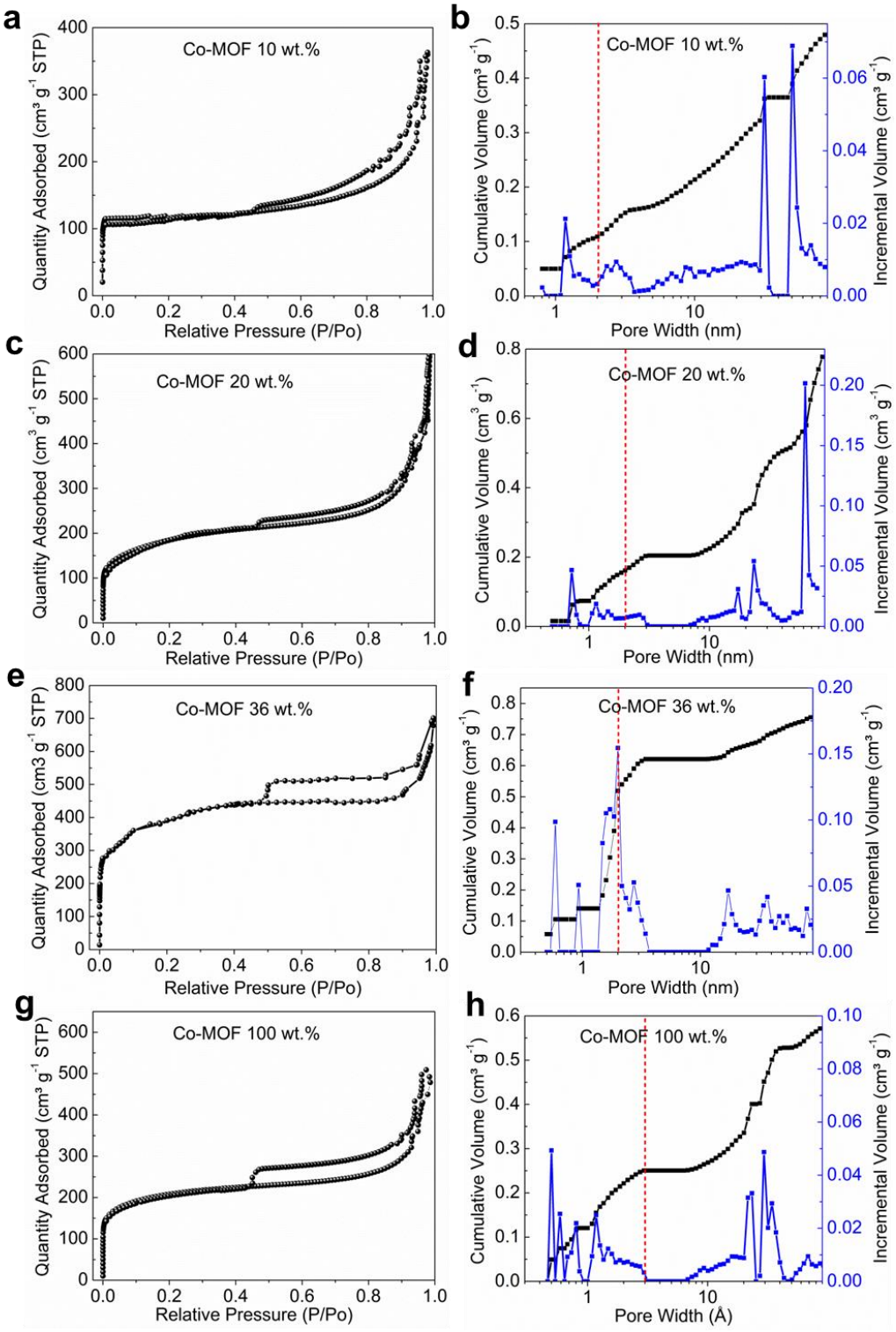

Supplementary Fig. 2| The comparison of BET surface area (**a, c, e, g**) and pore size distribution (**b, d, f, h**) for Co-N-GF samples with different CoMOF contents in the CoMOF/PAN fiber precursors.

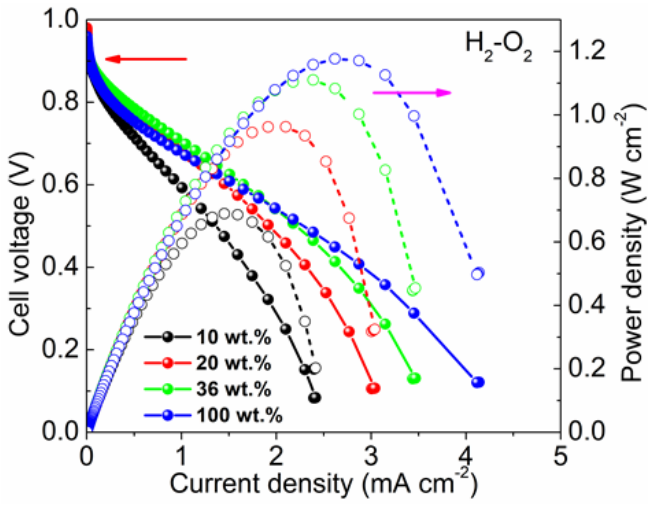

Supplementary Fig. 3| H_2-O_2 fuel cell performance of LPCNGF prepared with Co-N-GF obtained from various CoMOF contents in the CoMOF/PAN fiber precursors (denoted as Co-N-GF(x wt.%), where "x" indicates the content of Co-MOF. Fuel cell performance of LPCNGF prepared with Co-N-GF(100 wt.%), shows a higher current in the mass transport region, but lower current in the kinetic region relative to that of catalyst prepared with Co-N-GF(36 wt.%). The higher concentration of meso-pore and lower concentration of micro-pore in the Co-N-GF(100 wt.%) compared to Co-N-GF(36 wt.%) lead to a better mass transfer property but inferior kinetics. The inferior performances of catalysts prepared with Co-N-GF(10 wt.%), Co-N-GF(20 wt.%) relative to that of prepared with Co-N-GF(36 wt.%), originate from their lower Co-N_x PGM-free active sites concentration. Test condition: 80 ^{o}C, 100% RH, 150 KPa_{abs}, membrane = Nafion®211, anode loading ≤ 0.035 mg_{Pt} cm^{-2}, cathode Pt loading ≤ 0.056 mg_{Pt} cm^{-2}, H_2 flow rate = O_2 flow rate = 200 mL min^{-1}.

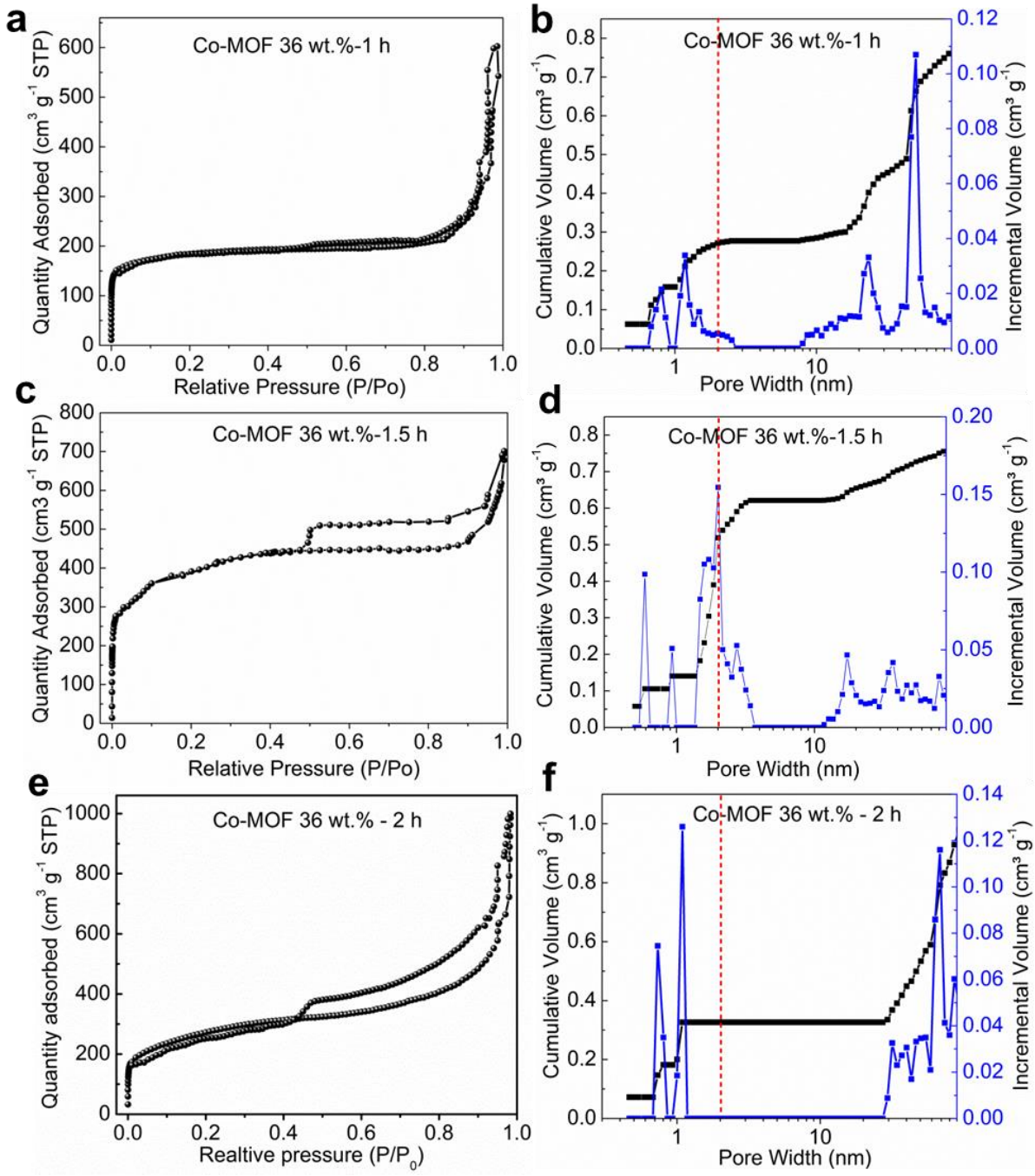

Supplementary Fig. 4| The comparison of BET surface area (**a, c, e**) and pore size distribution (**b, d, f**) for Co-N-GF (36 wt.%) pyrolyzed at 1000 ^{o}C for different times.

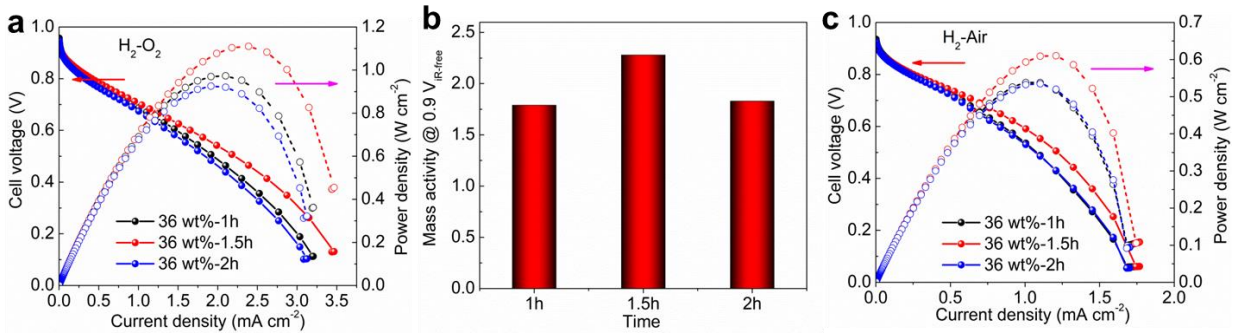

Supplementary Fig. 5| (**a**) H_2-O_2 fuel cell performances of LPCNGF prepared with Co-N-GF(36 wt%) obtained at 1000 ^oC for different pyrolysis times. (**b**) the corresponding MA at 0.9 $V_{iR\text{-}free}$ voltage. (**c**) H_2-Air fuel cell performances of LPCNGF prepared with Co-N-GF obtained at 1000 ^oC for different pyrolysis times. Test condition: 80 ^oC, 100% relative humidity RH, 150 KPa_{abs}, membrane = Nafion® 211, anode loading = 0.035 mg_{Pt} cm^{-2}, cathode Pt loading = 0.056 mg_{Pt} cm^{-2}, H_2 flow rate = O_2 flow rate = 200 mL min^{-1} in H_2-O_2 cell, and H_2 flow rate = 200 mL min^{-1} & Air flow rate = 780 mL min^{-1} in H_2-Air cell.

The micropore is essential for PGM-free catalyst to achieve high activity[1,2] and the mesopore is required for efficient mass transfer[3,4]. It should be emphasized that Co-MOF plays a critical role in tuning the micro/meso-pore structure and Co-N_x population of the final catalyst to achieve the highest ORR activity. To elucidate this point, we investigated the Co-MOF concentration in the Co-MOF/PAN fiber along with its pyrolysis time (Supplementary Fig. 2 and Fig. 4). With increasing concentrations of Co-MOF from 10% to 36%, the BET surface area of the obtained Co-N-GF increased from 393.3 to 824.7 m^2 g^{-1}, the volume of the micropore increased from 0.11 cm^3 g^{-1} to 0.53 cm^3 g^{-1} (Supplementary Table 1). A higher concentration of Co-MOF leads to better fuel cell performance (Supplementary Fig. 3). Next, we discussed the Co-MOF/PAN fiber with 36% Co-MOF concentration pyrolyzed at 1000 ^oC in Ar for 1 h, 1.5 h and 2 h. With prolonged pyrolysis time, even though the BET surface area increased to 1200 m^2 g^{-1}, the micropore volume decreased after 1.5 h (Supplementary Fig. 4, Supplementary Table 2), resulting in a lower fuel cell activity after 1.5 h (Supplementary Fig. 5). The mass activity of the

corresponding PEMFCs ranged from 1.78 to 2.28 A mg_{Pt}^{-1} (Supplementary Fig. 5**b**). The highest fuel cell activity was achieved with Co-N-CF(36 wt%) pyrolyzed for 1.5 h. Hence, after the optimization with CoMOF concentration of 36% in the CoMOF/PAN fiber, and pyrolysis time of 1.5 h in Ar, the obtained Co-N-GF exhibits a high BET surface area with high porosity possessing balanced micropore and mesopore structure in a well-defined network architecture.

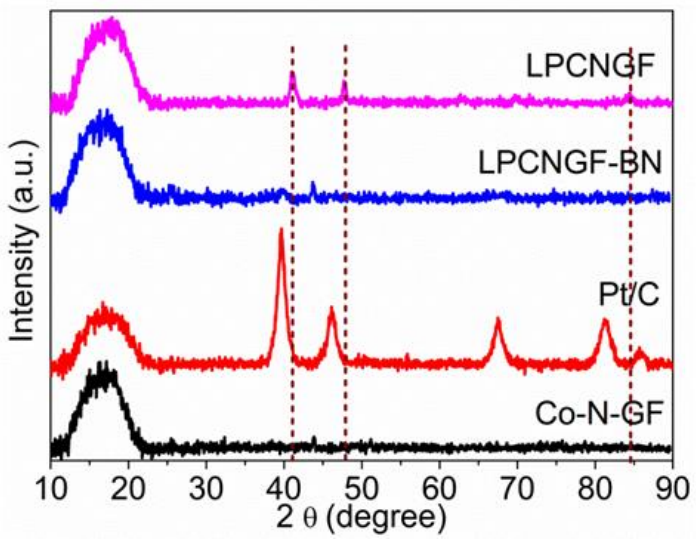

Supplementary Fig. 6| XRD patterns of LPCNGF at sequential stages of catalyst preparation: Co-N-GF, LPCNGF-BN (after Pt addition and before annealing in NH_3), LPCNGF (final catalyst). Commercial 40 wt.% of Pt/C was used as the reference of the pure Pt. The XRD pattern of Co-N-GF showed a small peak at 2 θ of 44.0^o ascribed to Co metal crystallites, indicating the small particle size of the generated Co crystals and the amorphous structure of other Co-bearing phases. For LPCNGF-BN, a weak and broad peak at 39.6^o assigned to Pt (111) was detected; indicating that the small particle size of the in-situ reduced Pt metal was dominated by the most active Pt (111) facet. After NH_3 treatment to form LPCNGF, XRD confirmed the formation of Pt-Co alloy. The peak at 44.0^o disappeared, suggesting that most of the Co metal crystals were alloyed with Pt. The Pt (111) peak was shifted toward high angles relative to Pt/C, confirming the formation of PtCo alloy, as well as Pt bond contraction[5].

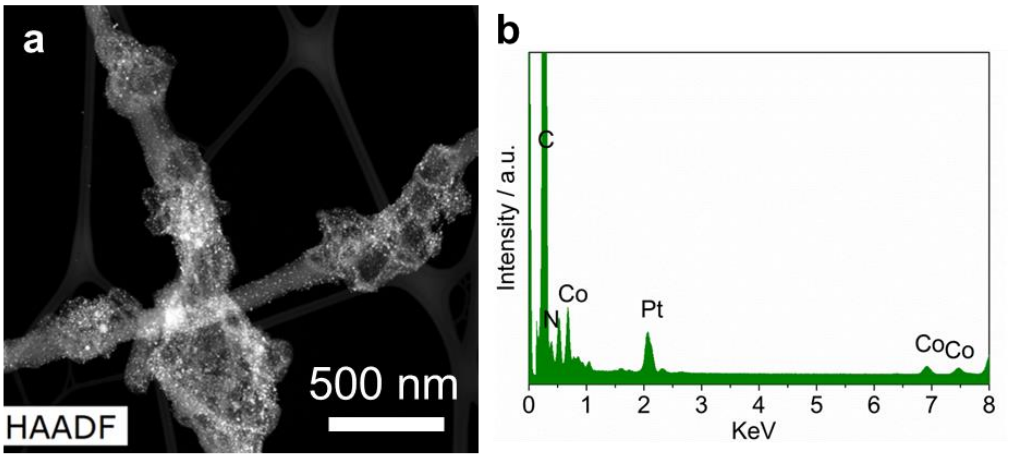

Element	at.%	Wt%
Carbon	94.0 ± 8	83.9 ± 0.9
Nitrogen	4.0 ± 0.5	4.0 ± 0.1
Cobalt	1.6 ± 0.2	6.8 ± 0.1
Platinum	0.4 ± 0.1	5.2 ± 0.1

Supplementary Fig. 7| (**a**) HAADF-STEM image of two single-fibers. (**b**) STEM-EDS elemental analysis. The spectrum was recorded from (**a**). The Co:Pt ratio represents an average value of multiple large areas of the sample. The average atomic ratios and weight ratios of C:N:Co:Pt are listed in the table.

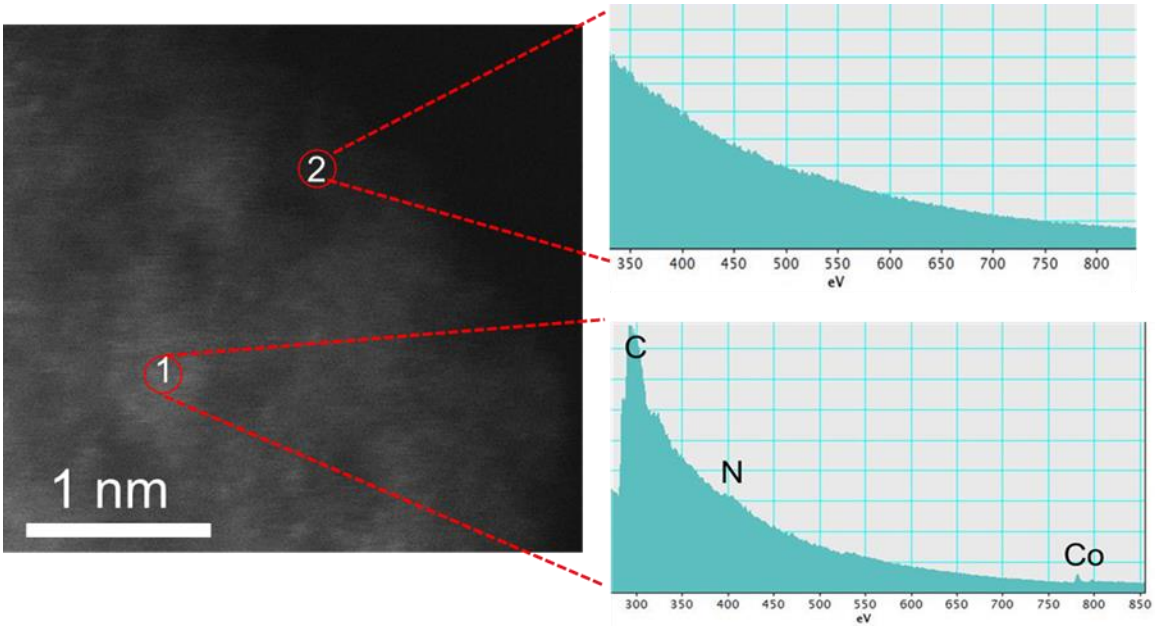

Supplementary Fig. 8| Atomic resolution HAADF-STEM image of carbon part in LPCNGF sample, and the EEL spectra of the N K-edge and Co L-edge acquired from the areas with (1) and without (2) bright dots, revealing that the single Co atoms were embedded in the carbon matrix presenting together with N.

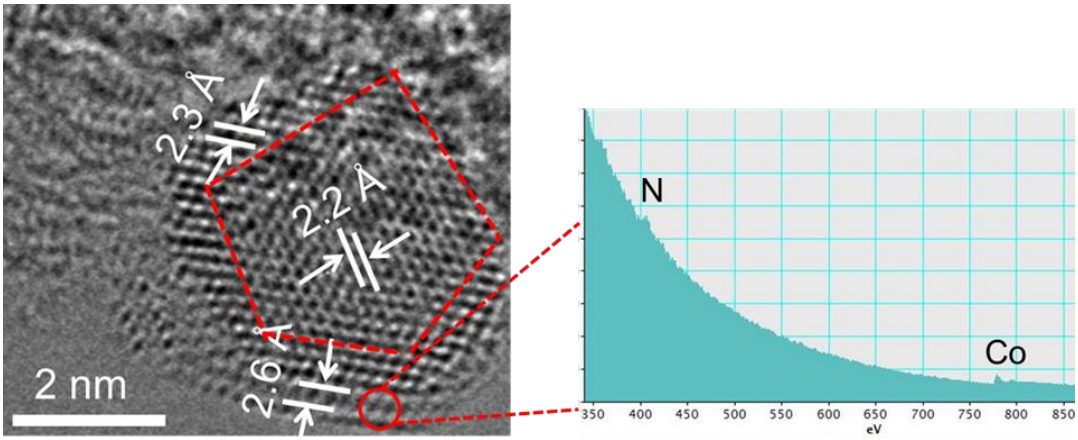

Supplementary Fig. 9| HRTEM image of individual PtCo core-shell alloy in LPCNGF, showing lattice spacing of PtCo core (2.2 Å), Pt skin (2.3 Å) and CoN/C terrace (2.6 Å). EEL spectrum acquired from the terrace in the red circle confirms that the composition consists of Co and N.

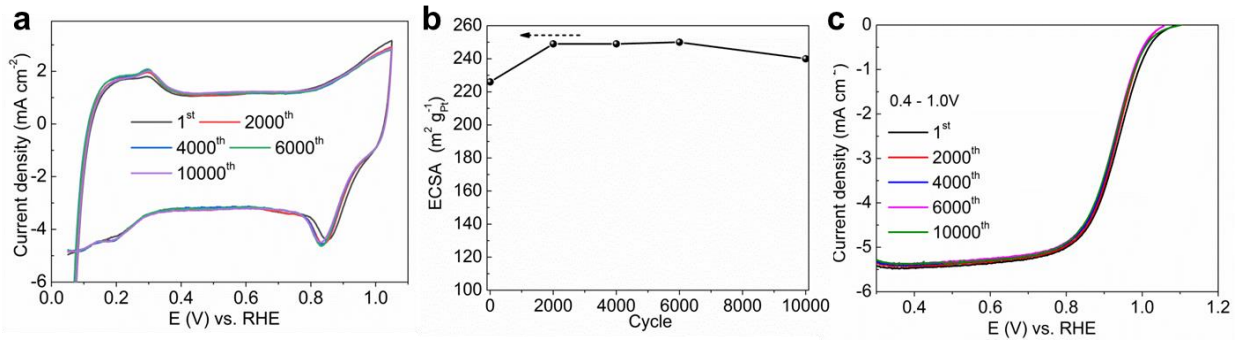

Supplementary Fig. 10| (**a**) CV curves of LPCNGF at selective cycles. (**b**) ECSA evolution of LPCNGF as function of the cycle numbers. (**c**) LSV curves of LPCNGF at selective cycles. The durability measurements were conducted by sweeping the potential between 0.4 V and 1.0 V by RRDE method in O_2 saturated 0.1 M $HClO_4$ electrolyte. Pt loading was ~ 4 μg cm^{-2}.

Electrochemical active surface area (ECSA) is believed to be an important contributor to catalyst activity. We calculate the ECSA of LPCNGF by measuring the charge collected in the H_{upd} absorption /desorption region after double-layer correction and assuming a value of 210 μc cm^{-2} for the absorption of a hydrogen monolayer[6]. At room temperature, the LPCNGF exhibited ECSA of 226 m^2 g_{Pt}^{-1} (Supplementary Fig. 10**b**). The high ECSA may result from the unique hierarchical porous structure of the interconnected nanofiber support that increases the accessibility of Pt to the reactant and ionomer, also shortens the ionic diffusion length in the electrode. The catalyst is very stable. We observed a slightly increase in ECSA (240 m^2 g_{Pt}^{-1}), and only 6 mV voltage loss in half-wave potential ($E_{1/2}$) after 10 000 cycles.

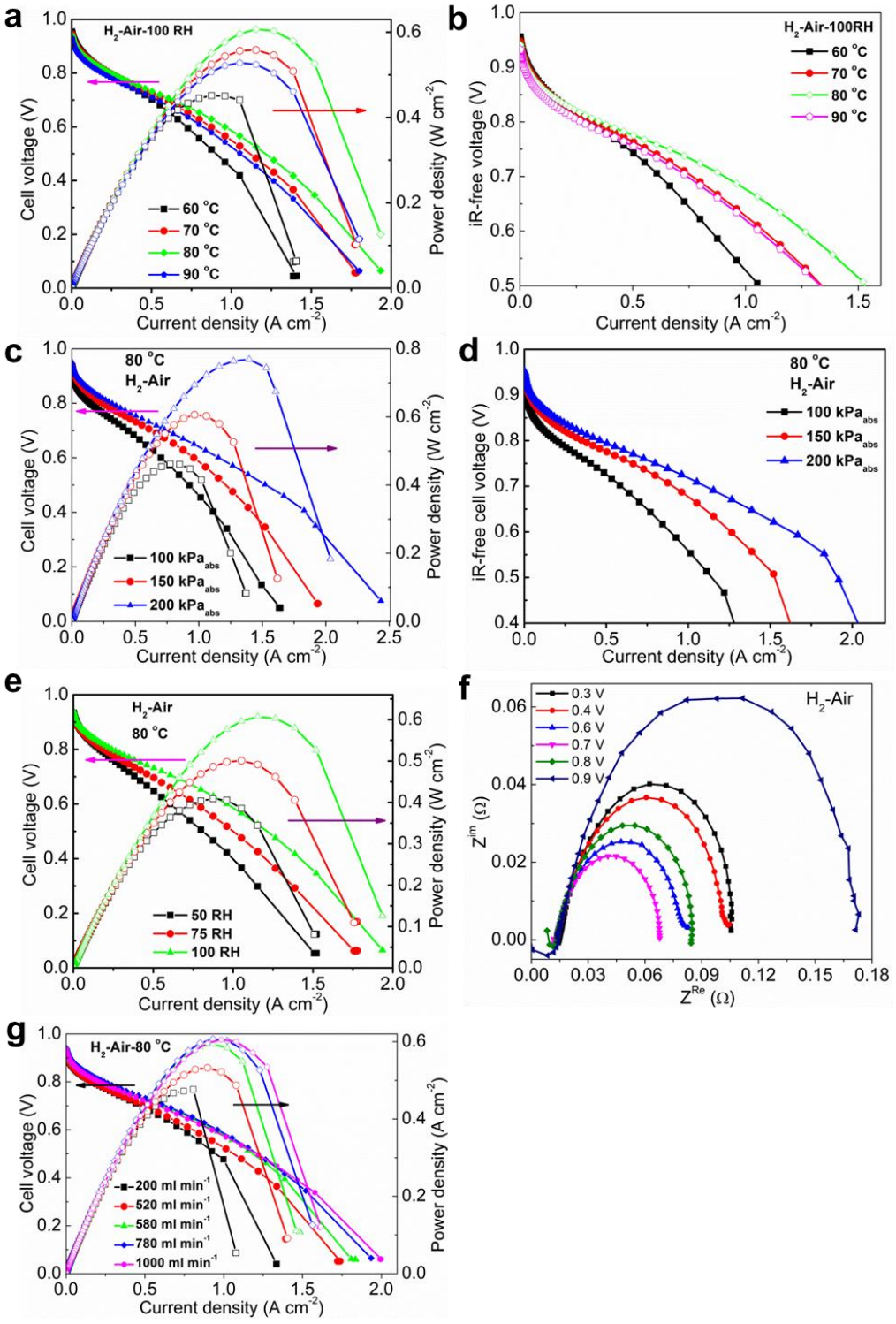

Supplementary Fig. 11| H_2-Air fuel cell performance investigations for MEA with LPCNGF as cathodic catalyst under different test condition, (**a**), 150 KPa_{abs}, 100%RH, different temperatures of 60 ^oC, 70 ^oC, 80 ^oC, 90 ^oC; (**b**), iR corrected polarization curves obtained from (**a**); (**c**) 80 ^oC, 100%RH, different pressure of 100 KPa_{abs}, 150 KPa_{abs}, 200 KPa_{abs}; (**d**) iR corrected polarization curves obtained from (**c**), showing the large current produced by LPCNGF.

(**e**) 80 ^{o}C, 150 KPa$_{abs}$, different RH of 50%, 75%, 100%; (**f**) 80 ^{o}C, 100%RH, 150 KPa$_{abs}$, 1-10000 Hz, EIS at different voltage of 0.3 V, 0.4 V, 0.6 V 0.7 V, 0.8 V, 0.9 V; (**g**), 80 ^{o}C, 150 KPa$_{abs}$, 100%RH, different Air flow rate of 200, 520, 580, 780 and 1000 ml min^{-1}. All the tests were conducted on the same MEA: membrane = Nafion®211, anode loading ≤ 0.035 mg$_{Pt}$ cm^{-2}, cathode Pt loading ≤ 0.056 mg$_{Pt}$ cm^{-2}, H_2 flow rate = 200 mL min^{-1}, air flow rate = 780 ml min^{-1} for (**a**) to (**f**).

We also studied the effects of various parameters including temperature, pressure, RH, and resistance on the fuel cell performance (Supplementary Fig. 11 and Fig. 12). The activities of both H_2-O_2 cell and H_2-Air cell were enhanced with increasing temperature from 60 ^{o}C to 80 ^{o}C, which is attributed to the increased gas diffusivity and membrane conductivity at higher temperature. Increasing temperature to 90 ^{o}C resulted in dry-out of the membrane and poor conductivity, manifesting itself as a performance decrease. Even at 60 ^{o}C, the MA of LPCNGF is still as high as 1.67 A g_{Pt}^{-1}. The MA of 2.28 A g_{Pt}^{-1} at 80 ^{o}C and 150 KPa$_{abs}$, is the highest ever achieved in an operating fuel cell (Supplementary Table 3). Fuel cell performances at different absolute pressure: 100 KPa$_{abs}$, 150 KPa$_{abs}$, 200 KPa$_{abs}$ were compared (Supplementary Fig. 11**c**, and Fig. 12**c**). As operating pressure increased, the fuel cell performance improved. The H_2-O_2 cell and H_2-Air cell reached maximum power densities of 1.36 W cm^{-2} and 0.77 W cm^{-2} at 200 KPa$_{abs}$, corresponding to an effective Pt utilization of 0.041 g_{Pt} kW^{-1} on the cathode in H_2-O_2 cell, and 13.8 kW g_{Pt}^{-1} in H_2-Air cell, suggesting a high efficiency of LPCNGF toward ORR in PEMFC. The results rank the highest reported so far (Fig. 4**e**).

Electrochemical impedance spectroscopy (EIS) has a significant impact on the electron transfer property of the support, and the higher catalytic performance is believed to be associated with an improved electrical conductivity. EIS data is represented as Nyquist plot extracted to be ohmic resistance (Rohm), charge transfer resistance (Rct) and mass transport resistance (Rmt). H_2-Air (Supplementary Fig. 11**f**) and H_2-O_2 cell (Supplementary Fig. 12**f**) cell show very low Rct and Rmt, displaying the high conductivity and excellent water management property of Co-N-GF support due to the formation of P-type graphene and the hierarchical interconnected meso-pores., We observed a decrease in limiting current density at low RH due to reduction in concentration of the reactant gas. Performance loss caused by the mass transport is barely noticeable at 100% RH (Supplementary Fig. 11**e** and Fig. 12**e**). H_2-Air fuel cell performance is improved as

increasing the air gas flow rate from 200 ml min^{-1} to 520 ml min^{-1} due to the increased O_2 concentration to the cathode layer, which increases the reaction rate. The increase in H_2-Air cell performance is not obvious from 580 ml min^{-1} to 1000 ml min^{-1}, implying that the rationally-designed porous structure compensates the mass transport limitation. We attribute the unprecedented fuel cell performance to the high surface area, the unique hierarchical porous interconnected-pore structure, the synergistic effect between PtCo alloy and Co-N-GF nanofiber PGM-free catalyst, contributing to the ORR simultaneously, and the excellent electron conductivity and corrosion resistance of the support.

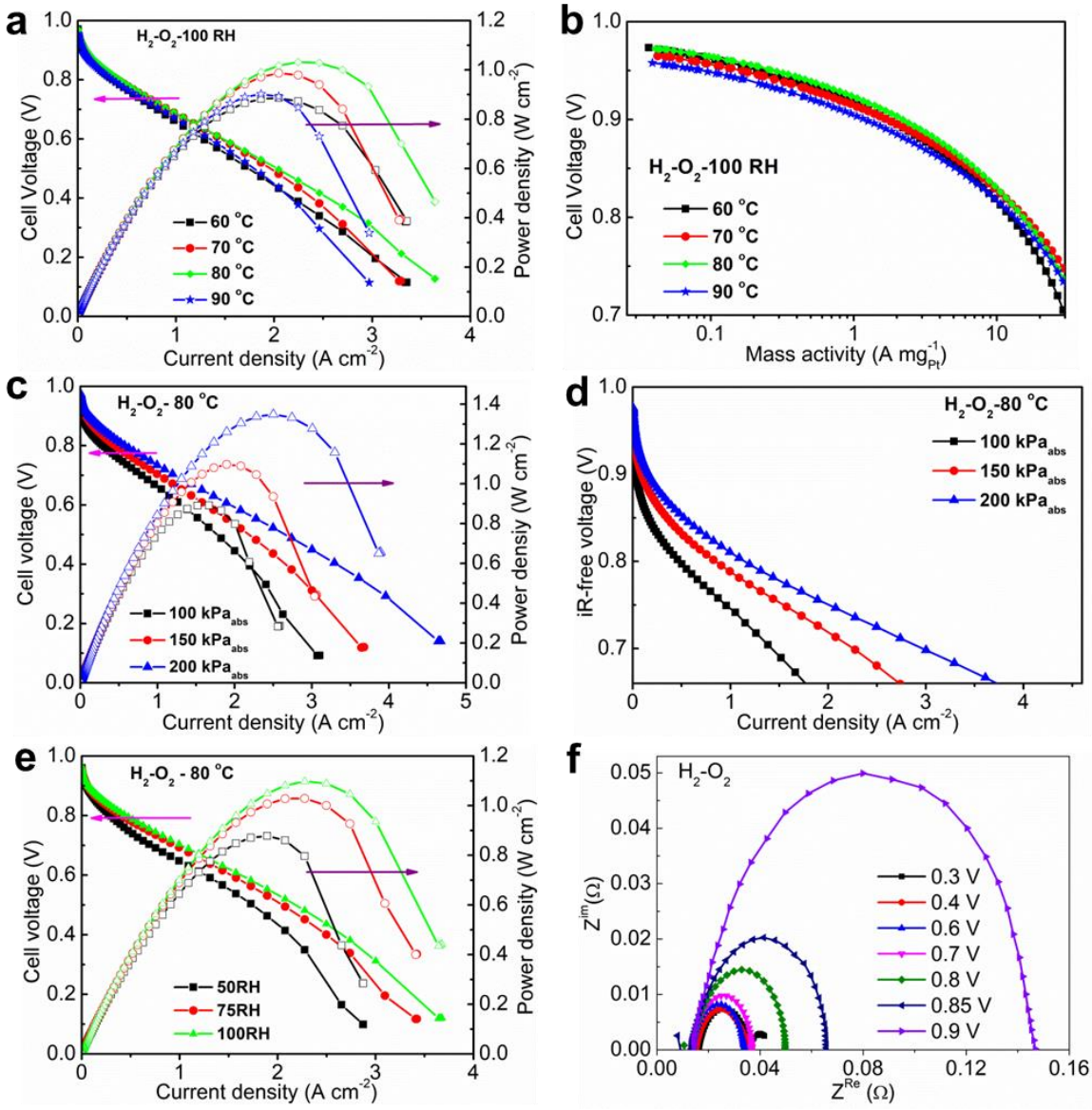

Supplementary Fig. 12| H_2-O_2 fuel cell performance investigations for MEA with LPCNGF as cathodic catalyst under different test condition, (**a**), 150 KPa_{abs}, 100%RH, different temperatures of 60 ^oC, 70 ^oC, 80 ^oC, 90 ^oC; (**b**), the corresponding Tafel plot of mass activity; (**c**) 80 ^oC, 100%RH, different pressure of 100 KPa_{abs}, 150 KPa_{abs}, 200 KPa_{abs}; (**d**) iR corrected polarization curves obtained from (**c**), showing the large current produced by LPCNGF; (**e**) 80 ^oC, 150 KPa_{abs}, different RH of 50%, 75%, 100%; (**f**) 80 ^oC, 100%RH, 150 KPa_{abs}, 1-10000 Hz, EIS at different voltage of 0.3 V, 0.4 V, 0.6 V 0.7 V, 0.8 V, 0.85 V, 0.9 V. The slightly high Rct + Rmt at 0.9 V is due to the membrane less hydrated at 0.9 V. All the tests were conducted on the same MEA: membrane = Nafion® 211, anode loading ≤ 0.035 mg_{Pt} cm^{-2}, cathode Pt loading ≤ 0.056 mg_{Pt} cm^{-2}, H_2 flow rate = O_2 flow rate = 200 mL min^{-1}.

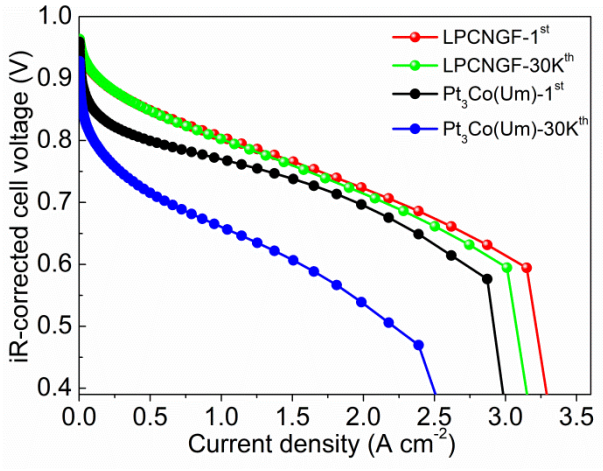

Supplementary Fig. 13| IR-corrected polarization curves of H_2-O_2 cell obtained from Fig. 4**c** in the main text, showing that LPCNGF possessing significant higher activity than that of Pt_3Co (Um) in the kinetic region > 0.78 V. No discernable degradation was observed for LPCNGF catalyst after 30,000 AST. However, the Pt_3Co (Um) was seriously degraded.

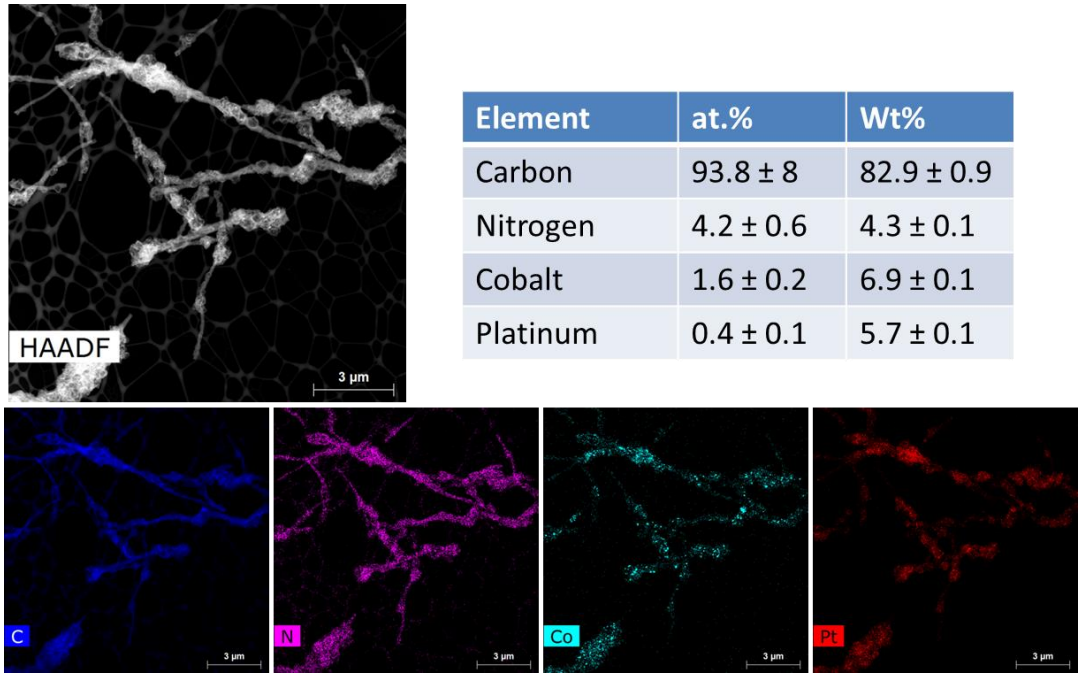

Element	at.%	Wt%
Carbon	93.8 ± 8	82.9 ± 0.9
Nitrogen	4.2 ± 0.6	4.3 ± 0.1
Cobalt	1.6 ± 0.2	6.9 ± 0.1
Platinum	0.4 ± 0.1	5.7 ± 0.1

Supplementary Fig. 14| HAADF-STEM image and the corresponding EDS elemental mapping of LPCNGF after AST in fuel cell. Sample was extracted from the cathode of the MEA after 30,000 AST test in H_2-Air cell and continued 30,000 AST test in H_2-O_2 cell. EDS elemental analysis averaged over multiple areas demonstrated that the atomic ratio and the weight ratio of C: N:Co:Pt after two consecutive ASTs in fuel cell were basically the same as the fresh sample, corroborating the stable structure of LPCNGF under harsh PEM conditions.

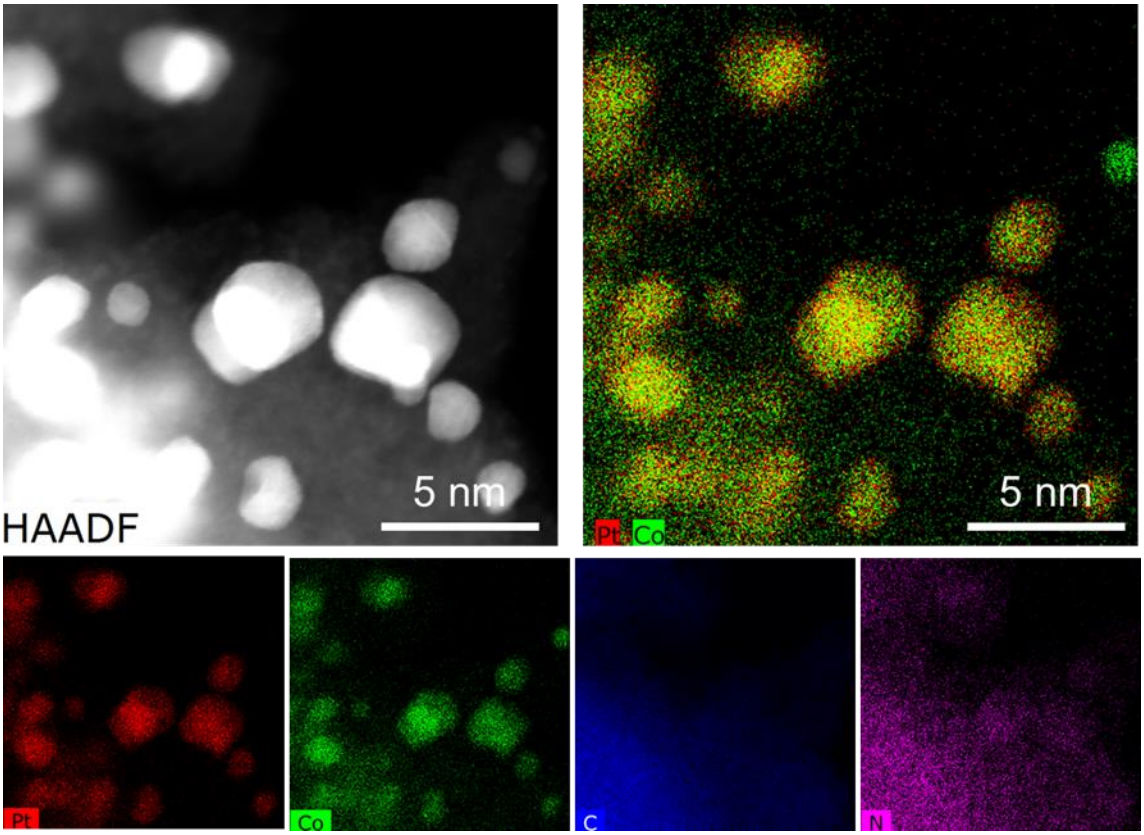

Supplementary Fig. 15| HAADF-STEM image focusing on PtCo alloy in the LPCNGF sample extracted from MEA after the 30,000 AST test in H_2-Air cell and continued 30,000 AST test in H_2-O_2 cell; corresponding EDS elemental mapping is also shown. The images revealed that the particle size of the alloy was preserved without agglomeration after the harsh AST test, further confirming the durable structure of the PtCo alloy and the intimate interaction between the alloy and the PGM-free Co-N-GF support in the LPCNGF sample.

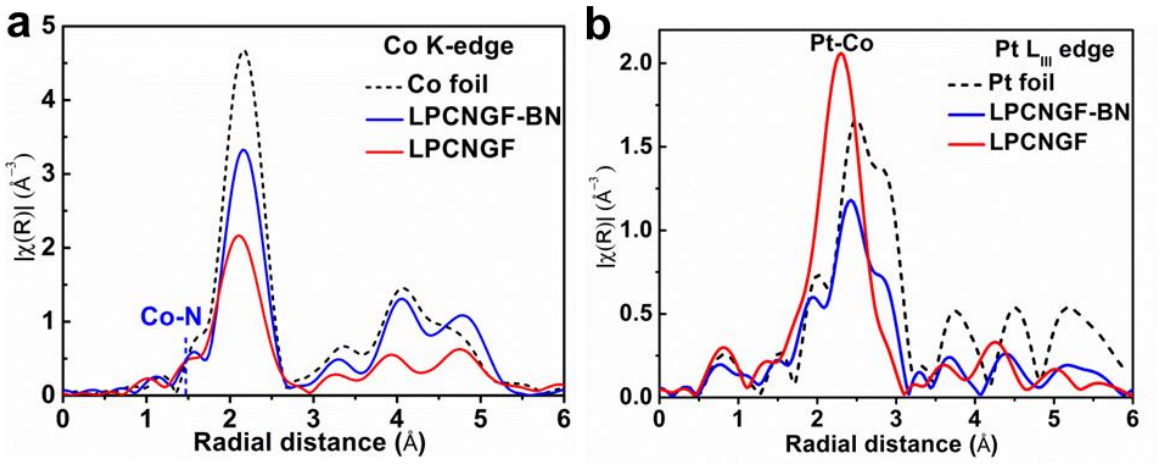

Supplementary Fig. 16| Fourier transforms of the EXAFS spectra at Co K-edge (**a**) and Pt L_{III}-edge (**b**) for LPCNGF before (LPCNGF-BN) and after NH_3 treatment, as well as the references.

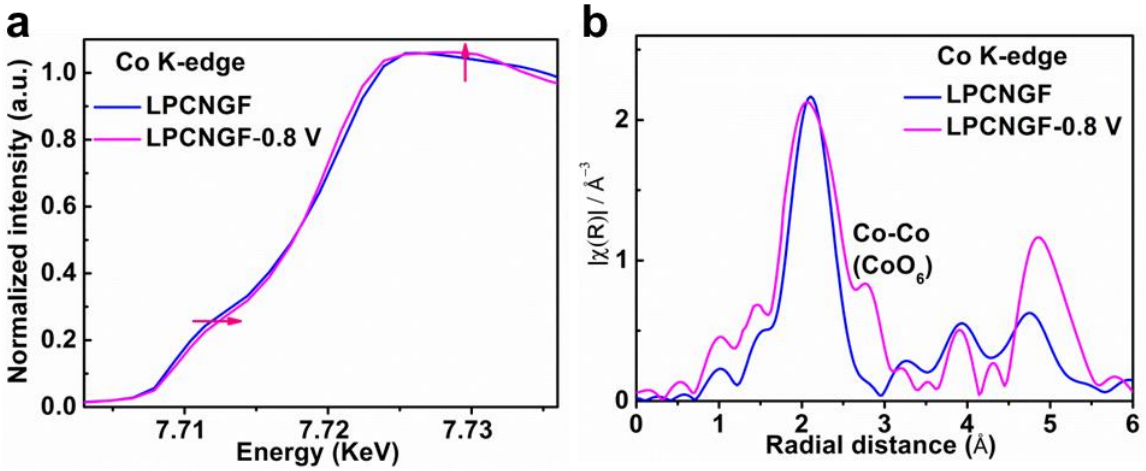

Supplementary Fig. 17| (**a**) XANES and (**b**) EXAFS spectra at Co K-edge for the LPCNGF (ex-situ sample) and LPCNGF-0.8 V (in-situ sample at applied potential of 0.8 V). The EXAFS spectrum at Co K-edge of the in-situ sample is different from that of the ex-situ sample.

Table S1. BET surface areas and pore volume distribution of Co-N-GF obtained from different Co-MOF content in the Co-MOF/PAN fiber precursors, which were pyrolyzed at 1000 ^{o}C for 1.5 h in flowing Ar.

CoMOF content	BET Surface Area (m^2 g^{-1})	$V_{Micropore}$ (cm^3 g^{-1})	$V_{Mesopore}$ (cm^3 g^{-1})	$V_{Macropore}$ (cm^3 g^{-1})
10 wt.%	393.3	0.11	0.24	0.27
20 wt.%	629.4	0.17	0.35	0.25
36 wt.%	824.7	0.53	0.19	0.13
100 wt.%	698.3	0.25	0.28	0.21

Table S2. BET surface areas and pore volume distribution of Co-N-GF obtained from 36% Co-MOF content in the Co-MOF/PAN fiber precursor followed by pyrolysis in flowing Ar at 1000 ^{o}C for various times periods.

Time of pyrolysis	BET Surface Area (m^2 g^{-1})	$V_{Micropore}$ (cm^3 g^{-1})	$V_{Mesopore}$ (cm^3 g^{-1})	$V_{Macropore}$ (cm^3 g^{-1})	Co wt.%
1 h	614.7	0.28	0.32	0.24	9 ~ 11
1.5 h	824.7	0.53	0.19	0.13	6 ~ 8
2 h	1200.0	0.33	0.17	0.6	10 ~ 12

Table S3. Comparisons of ORR performance of LPCNGF with recently reported Pt-based catalysts both in RDE and operating fuel cell.

Catalyst	RRDE				PEM Fuel cell							Ref.
	MA (A mg_{Pt}^{-1})	SA (mA cm^{-2})	ECSA (m^2 g_{Pt}^{-1})	Durability loss in MA (%)	Anode Pt loadings (mg cm^{-2})	Cathode Pt loadings (mg cm^{-2})	MA@0.9V BOL(A cm^{-2})	MA@0.9V EOL(A cm^{-2})	Voltage loss at 0.8 A cm^{-2} (mV)	Current at 0.8V (H_2-Air cell) (mA cm^{-2})	Pt utilization 150 KPa (kW g_{Pt}^{-1})	
LPCNGF	**5.08**	**22.2**	**226**	**10 K, 14%**	**0.035**	**0.056**	**2.28**	**1.96**	**0**	**438**	**11.1 (80 °C)**	**This work**
DOE					**Total 0.125**		**0.44**	**0.26 (≤ 40%)**	**≤ 30**	**≥300**	**8**	**7**
PtCo/HSC-f					0.025	0.06	0.7	TBD	TBD	382	10.6 (94 °C)	8
PtCo/HSC-e					0.025	0.1	0.6	40% in loss	20	306	7.1 (94 °C)	8
Pt@CS@CNF900	0.1167[a]		178[a]		0.1	0.125	NA	NA	+1%	NA	NA	9
PtNiCo NWs	4.20	5.11	82.2	30k, 21.4%	0.05	0.1						10
Pt-Ni NPs					0.05	0.1	0.62	0.56	~ 30	125		11
Pt/N-KB 900°C					~0.15	~0.11	0.202	0.199		~250		12
LP@PF-2	12.36		150		0.35	0.043	1.87	0.266				13
LP@PF-2					0.35		1.1	0.98				13
L10-CoPt/Pt	2.26	8.26	27.3		0.105	0.105	0.56	0.45	~ 20	~ 280		14
PtNi-BNCs	3.52	5.16	68.2	50K, 1.1%	0.1	0.15	NA	NA				15
Jagged Pt NW	13.6	11.5	118	10K, 12%								16
PtPb/Pt plate	4.3	7.8	55.1	50k, 7.7%								17
Pt–CoO heat 2	8.37 ± 0.55	5.38 ± 0.21	156 ± 4									18
PtPb/PtNi IM	1.92	5.16	37.2	10K,17.2%								19
Pt_3Fe NW	2.11	4.34	34.0	50K,24.6%								20

Supplementary References

1 Jaouen Fdr., Lefe`vre M., Dodelet J. -P., Cai M., Heat-treated Fe/N/C catalysts for O_2 electroreduction: Are active sites hosted in micropores? *J. Phys. Chem. B.* **110**, 5553-5558 (2006).

2 Jaouen Fdr., *et al.* Cross-laboratory experimental study of non-noble-metal electrocatalysts for the oxygen reduction reaction. *ACS Appl. Mater. Interfaces* **1**, 1623-1639 (2009).

3 Ignaszak A., Ye S., Gyenge Ed., A Study of the catalytic interface for O_2 electroreduction on Pt: the interaction between carbon support meso/microstructure and ionomer (Nafion) distribution. *J. Phys. Chem. C* **113**, 298-307 (2008).

4 Antolini E., Carbon supports for low-temperature fuel cell catalysts. *Appl. Catal. B* **88**,1-24 (2009).

5 Strasser P., *et al.* Lattice-strain control of the activity in dealloyed core-shell fuel cell catalysts. *Nat. Chem.* **2**, 454-460 (2010).

6 Gloaguen F., Leger J. -M., Lamy C., Electrocatalytic Oxidation of Methanol on Platinum Nanoparticles Electrodeposited onto Porous Carbon Substrates. *J. Appl. Electrochem.* **27**, 1052-1060 (1997).

7 DOE FCTTR. US DRIVE Partnership. Fuel Cell Technical Team Roadmap, November 2017, https://www.energy.gov/sites/prod/files/2017/11/f46/FCTT_Roadmap_Nov_2017_FINAL.pdf. (2017).

8 Kongkanand A., Annual Merit Review DOE Hydrogen and Fuel Cells and Vehicle Technologies Programs, Washington, DC, 2018, https://www.hydrogen.energy.gov/pdfs/review18/fc144_kongkanand_2018_o.pdf.

9 Karuppannan M., *et al.* A highly durable carbon-nanofiber-supported Pt–C core–shell cathode catalyst for ultra-low Pt loading proton exchange membrane fuel cells: facile carbon encapsulation. *Energy. Environ. Sci.* **12**, 2820-2829 (2019).

10. Jiang K., *et al.* Efficient oxygen reduction catalysis by subnanometer Pt alloy nanowires. *Sci. Adv.* **3**, 1601705 (2017).

11. Han B., *et al.* Record activity and stability of dealloyed bimetallic catalysts for proton exchange membrane fuel cells. *Energy. Environ. Sci.* **8**, 258-266 (2015).

12. Ott S., *et al.* Ionomer distribution control in porous carbon-supported catalyst layers for high-power and low Pt-loaded proton exchange membrane fuel cells. *Nat. Mater.* **19**, 77-85 (2020).

13. Chong L., *et al.* Ultralow-loading platinum-cobalt fuel cell catalysts derived from imidazolate frameworks. *Science* **362**, 1276-1281 (2018).

14. Li J., *et al.* Hard-Magnet L_{10}-CoPt Nanoparticles Advance Fuel Cell Catalysis. *Joule* **3**, 124-135 (2019).

15. Tian X., *et al.* Engineering bunched Pt-Ni alloy nanocages for efficient oxygen reduction in practical fuel cells. *Science* **366**, 850-856 (2019).

16. Li M., *et al.* Ultrafine jagged platinum nanowires enable ultrahigh mass activity for the oxygen reduction reaction. *Science* **354**, 1414-1419 (2016).

17. Bu L., *et al.* Biaxially strained PtPb/Pt core/shell nanoplate boosts oxygen reduction catalysis. *Science* **354**, 1410-1414 (2016).

18. Sievers G. W., *et al.* Self-supported Pt-CoO networks combining high specific activity with high surface area for oxygen reduction. *Nat. Mater.* **20**, 208-213 (2020).

10. Bu L., *et al.* PtPb/PtNi Intermetallic Core/Atomic Layer Shell Octahedra for Efficient Oxygen Reduction Electrocatalysis. *J. Am. Chem. Soc*. **139**, 9576-9582 (2017).

20. Luo M., *et al.* Stable High-Index Faceted Pt Skin on Zigzag-Like PtFe Nanowires Enhances Oxygen Reduction Catalysis. *Adv. Mater*. **30**, 1705515 (2018).